

Simultaneous Single-Shot Two-Dimensional Imaging of Nanoparticles and Radicals in Turbulent Reactive Flows

Yihua Ren,^{1,2} Yiyang Zhang,³ and Shuiqing Li^{1,*}

¹Key Laboratory for Thermal Science and Power Engineering of Ministry of Education, Department of Energy and Power Engineering, Tsinghua University, Beijing 100084, China

²Institute for Combustion Technology, RWTH Aachen University, Templergraben 64, Aachen 52056, Germany

³Key Laboratory of Advanced Reactor Engineering and Safety of Ministry of Education, Collaborative Innovation Center of Advanced Nuclear Energy Technology, Institute of Nuclear and New Energy Technology, Tsinghua University, Beijing 100084, China

(Received 13 August 2019; revised manuscript received 1 December 2019; accepted 14 February 2020; published 1 April 2020)

Recently, a phase-selective laser-induced breakdown spectroscopy (PS-LIBS) technique has been proposed and developed to diagnose nanoparticles. However, only a few kinds of nanoparticles can generate sufficient strong PS-LIBS signals for single-shot two-dimensional measurement. In this work, we report on the development and validation of a resonance-enhanced PS-LIBS for instantaneous two-dimensional imaging of nanoparticle formation and transport in a turbulent reactive flow. By matching the laser pulse with the absorption line of titanium atoms in the laser-induced nanoplasm, we find that the resonance-enhanced titanium atomic emissions are 1 order of magnitude stronger than the nonresonant spectra ranging from 498 to 502 nm. Based on the spectral characterization, a quantitative relation between the spectra and the particle volume fraction is theoretically established and validated by experiments. Combining the resonance-enhanced PS-LIBS and planar laser-induced fluorescence (PLIF) techniques, instantaneous two-dimensional distributions of the nanoparticle and the hydroxyl radical (OH radical) can be measured *in situ* in a turbulent reactive flow. The simultaneous measurement demonstrates a strong correlation between the nanoparticle formation and the reactive flow pattern in the turbulent region. The correlation further reveals that the precursor consumption is dominated by the turbulence effect, indicating the precursor chemistry-turbulence coupling.

DOI: 10.1103/PhysRevApplied.13.044002

I. INTRODUCTION

The formation and transport of nanoparticles are ubiquitous in various important physical processes such as soot inception [1], atmospheric aerosol formation [2,3], and interstellar dust evolution [4]. They are also of engineering significance. In the rising industry of nanotechnology, the gas-phase synthesis routes, e.g., flame synthesis [5,6], laser ablation [7], electric discharges [8], have shown great advantages in the scalability and versatility. However, the underlying physics governing the nanoparticle formation and transport in turbulent reactive flows are largely unknown. This limits the optimization of scalable synthesis processes and the capability of tailoring structures and morphologies of nanomaterials. Therefore, *in situ* nonintrusive diagnostics are highly desired for the investigation of nanoparticle formation and transport in turbulent reactive flows.

Several laser diagnostics methods have been developed for nanoparticle measurements. Specifically, laser-induced incandescence (LII) is widely adopted to measure the particle volume fraction (PVF) and size of soot, but LII is difficult to extend to metal and metal oxides owing to the complicate laser-absorption model and accommodation coefficients [9,10]. Laser-induced Rayleigh scattering (or elastic light scattering) is good for qualitative measurements, but the quantitative diagnostic is limited by the complex dependency of the signal intensity on both the particle size and structure, and concentration [11]. Small-angle x-ray scattering, based on Porod's law, is able to measure the size and fractal dimension of nanoparticles [12]. Coherent Rayleigh-Brillouin scattering is able to detect nanoparticles smaller than 10 nm [13,14]. Laser-induced fluorescence (LIF) is applied to measure important intermediate species in flame synthesis like SiO in the synthesis process of SiO₂ nanoparticles [15]. However, LIF cannot provide information about the particle-phase composition, which limits a comprehensive understanding of

*lishuiqing@tsinghua.edu.cn

nano particle formation and transport in turbulent reactive flows.

Recently, phase-selective laser-induced breakdown spectroscopy (PS-LIBS) was discovered [16] and developed to a diagnostic technique for tracing the gas-to-particle conversion of different elements [17,18] and measuring particle volume fraction [19]. PS-LIBS is a type of atomic emission spectroscopy generated from laser-induced nanoplasm during the laser-cluster interaction. The nanoplasm is initiated through an absorption-ablation-excitation process [20]. In the presence of a laser beam, electrons are excited to the conduction band through absorption, and then transfer the laser energy to crystal lattice via collision. The nanoparticle is then atomized and ablated into the nanoplasm forming atomic emissions. Different from millimeter-sized plasma in conventional LIBS, the nanoplasm has the lifetime of about 10^1 ns and the electron temperature of less than 10^4 K [16]. Within the nanosecond lifetime, the low kinetic energy of electrons makes the impact ionization of surrounding gas molecules difficult to happen. Therefore, the nanoplasm is confined locally around each single nanoparticle without visible sparks and strong Bremsstrahlung spectrum in both ultra-violet and visible ranges. This feature enables a two-dimensional laser-induced breakdown of nanoaerosols to visualize the nanoparticle distributions [17]. Unfortunately, in the weakly ablated nanoplasm with the low electron temperature [16], only a few elements can generate sufficiently strong atomic emissions for instantaneous two-dimensional measurements. This is because the spectral line intensity depends not only on the plasma temperature and the species concentration, but also on the atom characteristics like the transition probability, the degeneracy, and the upper energy level. Previous attempts to further enhance the atomic emission in the nanoplasm has been performed by Xiong *et al.* [21,22], showing the feasibility of the resonance-enhanced PS-LIBS

in point measurements. However, the relation between the resonance-enhanced PS-LIBS signal and nanoparticles was not established, and the application to instantaneous two-dimensional measurements of nanoparticles is still absent.

In this study, we achieve *in situ* instantaneous two-dimensional laser diagnostic of TiO_2 nanoparticles by applying the resonance-enhanced PS-LIBS technique. The technique is first characterized by one-dimensional spectral measurement. Then, a quantitative correlation between resonance-enhanced PS-LIBS signal and particle volume fraction is established theoretically and validated by experiments. Finally, the technique is utilized for instantaneous measurements of nanoparticles in a turbulent reactive flow. Together with simultaneous planar laser-induced fluorescence (PLIF) of OH radicals, the measurements elucidate the nanoparticle formation and transport mechanism in the turbulent reactive flow.

II. EXPERIMENTAL SETUP

In this work, a jet-diffusion flame is used to generate nanoparticles, as shown in Fig. 1(a). In laminar flow conditions, a multielement diffusion flame is used to stabilize the central jet-diffusion flame. In turbulent flow conditions, a cold sheath flow of pure air is introduced to increase the shear rate. The high shear rate causes the Kelvin-Helmholtz instability that severely disturbs the nanoparticle formation and transport in the central reactive flow. Details about the reactor and the operation conditions can be found in the Supplemental Material [23]. Titanium isopropoxide [TTIP, $\text{Ti}(\text{C}_3\text{H}_7\text{O})_4$, Sigma-Aldrich] is used as a precursor for the synthesis of TiO_2 nanoparticles. The precursor is heated to 363 K in a bubbler, carried by the oxygen gas flow, and fed into the flame. Depending on the precursor loading rates and gas-flow rates, the precursor concentration is adjusted from 1 to 100 ppm, and the

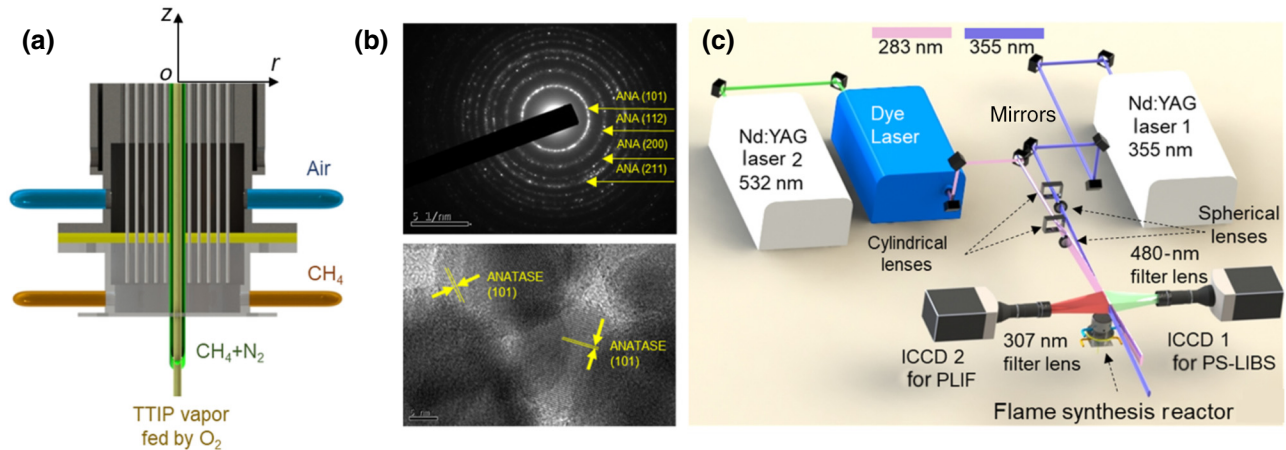


FIG. 1. (a) Schematic of the jet-diffusion burner; (b) TEM images of the synthesized nanoparticles; (c) schematic of the laser diagnostic setup.

particle volume fraction is varied from 1 to 1000 ppb. A water-cooled plate is placed at the height of 120 mm above the burner to collect synthesized nanoparticles. The plate is controlled at a low temperature about 78 °C to enhance the thermophoretic deposition of nanoparticles and to suppress the on-substrate sintering of nanoparticles. The TEM images in Fig. 1(b) show that the collected nanoparticles have an average size of about 31 nm with a geometric standard deviation of 1.36. The nanoparticles have the anatase crystalline structure as identified by the diffraction pattern.

The laser diagnostic system for simultaneous resonance-enhanced PS-LIBS and PLIF measurement is shown in Fig. 1(c). An Nd:YAG laser (Spectra-Physics, Quanta-Ray Lab 290) operated at the third harmonic is used to generate one laser beam with the wavelength of 354.71 nm (in air) for the resonance-enhanced PS-LIBS measurement. The laser beam is extended by a quartz cylindrical concave lens ($f = -400$ mm) and then focused by a spherical convex lens ($f = 500$ mm) to form a laser sheet with a beam waist of about 0.17 mm. Another Nd:YAG laser (Spectra-Physics, Quanta-Ray) operated at the second harmonic is used to pump a Sirah Cobra-Stretch tunable dye laser (Rhodamine 590 dye) for OH PLIF measurement. The laser wavelength is 282.93 nm (in air), and the laser energy is 4.2 mJ/pulse. The 282.93-nm laser beam is extended by a cylindrical concave lens ($f = -50$ mm) and focused by a spherical convex lens ($f = 300$ mm) to form a laser sheet with a beam waist of about 0.22 mm. Both laser beams have pulse durations of about 10 ns. The two lasers are operated at the same frequency of 5 Hz and synchronized by a digital delay generator (Stanford Research Systems, DG-645).

For the resonance-enhanced PS-LIBS, the spectrum at 480.54 nm is collected by an intensified charge-coupled device (ICCD) camera (Princeton Instrument, PI-MAX 4, P43 phosphor) equipped with a Nikon lens (MACRO 100F2.8D) and a bandpass filter (center wavelength of 480 nm and the FWHM of 10 nm). The spatial resolution is 0.0445 mm/pixel, and the depth of field about 0.8 mm. The two-dimensional OH fluorescence is recorded by another ICCD camera (Princeton Instrument, PI-MAX 4, P46 phosphor) opposite to the resonance-enhanced PS-LIBS camera, as shown in Fig. 1(c). The camera for OH fluorescence is fitted with a CERCO UV lens (94F4.1 type 2085) equipped with a bandpass filter (center wavelength of 307 nm with the FWHM of 10 nm). The spatial resolution is 0.0396 mm/pixel, and the depth of field is about 1 mm. The ICCD gate for resonance-enhanced PS-LIBS signal is set to be 200 ns with 128 ns prior to the laser pulse. The gate signal further triggers the other ICCD for OH PLIF measurement with the gate width of 200 ns.

Before two-dimensional measurement, one-dimensional spectral diagnostic is conducted to characterize the resonance-enhanced PS-LIBS signal. In this case, the 355-nm laser beam is focused by a spherical convex lens ($f =$

500 mm) into a laser line. The emitted spectra are then collected by two 400-mm focal-length achromatic lenses and an image rotator into a spectrometer (Princeton Instrument, ISO-PLANE 320) with a 2400 groove/mm holographic grating.

III. RESULT AND DISCUSSION

A. Characterization of resonance-enhanced PS-LIBS

In the presence of the 355-nm laser pulse, several distinct peaks (around 373, 480, and 500 nm) are identified as the atomic and ionic emissions of titanium by the one-dimensional spectral measurement, as shown in Fig. 2(a). The center wavelength and FWHM of the major spectra are listed in Table I of Appendix A and compared with the NIST database in the Supplemental Material [23]. The ionic spectral lines at 368.52, 375.93, and 376.13 nm are significantly enhanced in comparison with the same spectra in the presence of 532-nm laser pulses[19], indicating a stronger ionization degree of nanoplasma. Different from the two-photon absorption of the 532-nm laser pulse, the TiO₂ nanoparticles can directly absorb the 355-nm photons. Referring to the classical semiconductor theory [25], the interband transition rate can be estimated by

$$\frac{\partial N_e}{\partial t} = \frac{\alpha I}{h\nu} V_p, \quad (1)$$

where N_e is the number of conduction-band electrons generated by one nanoparticle, α is the interband absorption coefficient, I is the laser intensity, V_p is the nanoparticle volume, and $h\nu$ is the photon energy. Considering that the direct-allowed interband transition coefficient is about 4.7×10^4 cm⁻¹ [26], the laser pulse with the energy of 1 GW/cm² can generate about 2.2×10^4 conduction-band electrons in the first nanosecond for a 10-nm nanoparticle. This value is of 2 to 3 orders of magnitude larger than that generated in the two-photon absorption process [17,20]. The electrons are excited to the conduction band through the direct absorption of laser light, and then efficiently absorb the laser energy and transfer it to the crystal lattice via collision, which leads to the ablation of nanoparticles and the formation of nanoplasmas. It should be noted that the continuous bremsstrahlung spectrum is not observed in both ultra-violet and visible ranges, as the nanoplasma has a low electron temperature [16]. Thus, the impact ionization of surrounding gas molecules is difficult to happen and the nanoplasma remains localized around each nanoparticle without any visible sparks. In this case, the laser-induced breakdown only occurs for the nanoparticle rather than the gas molecules, which achieves a spark-free phase-selective breakdown.

After the ablation of nanoparticles, the same laser pulse also excites the metastable Ti atoms in the nanoplasma inducing the resonance-enhanced atomic emissions, which

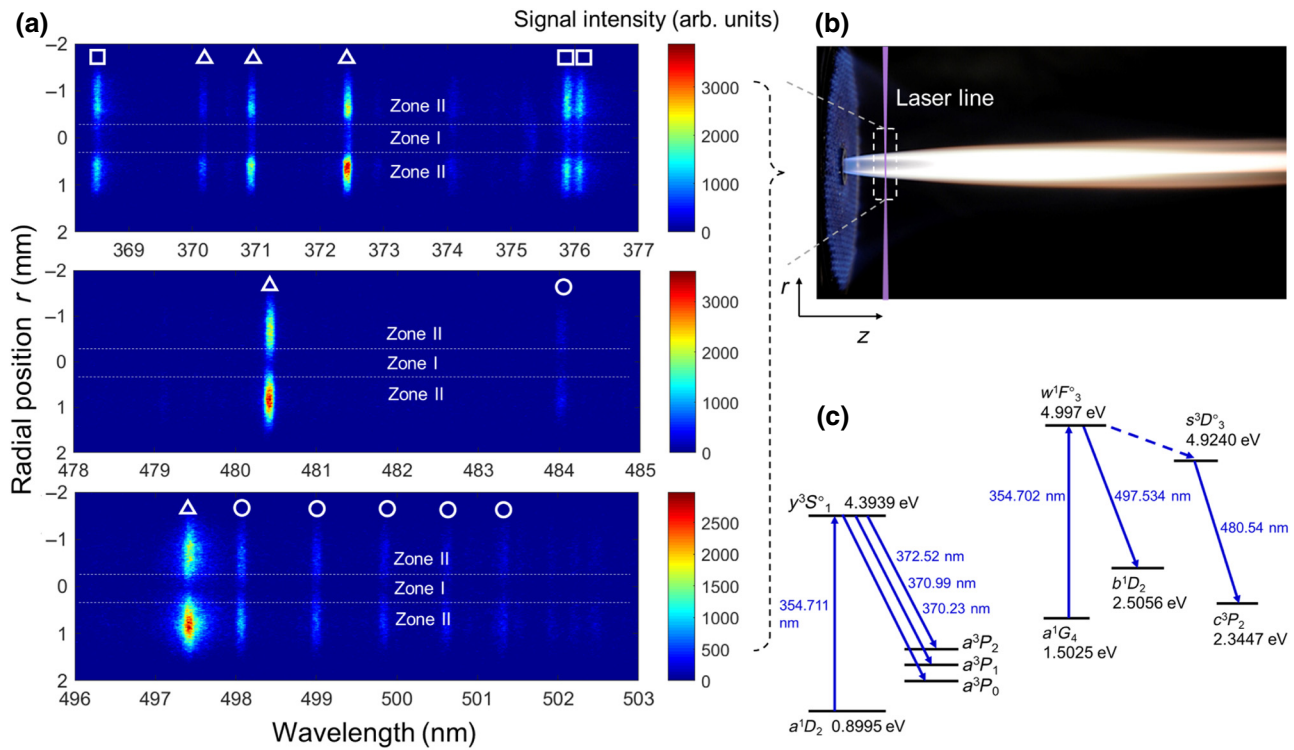


FIG. 2. (a) Atomic emissions in one-dimensional spectral measurement. White triangles and circles indicate resonance-enhanced and nonresonant atomic emissions of Ti, respectively, while the squares indicate ionic emissions. (b) Image of the flame synthesis reactor and the laser line, where r and z indicate the radial and axial directions. (c) Atomic energy diagram of the resonance-enhanced atomic emissions of Ti (the demonstrated wavelength is the Ritz wavelength in air according to the NIST database [24]).

is equivalent to a laser-induced fluorescence process. The resonant excitation is identified by scrutinizing the atomic energy diagram, as shown in Fig. 2(c). The laser wavelength 354.71 nm (in air) matches two absorption lines of Ti at 354.711 and 354.702 nm. The first one corresponds to the transition term of Ti (I) from a^1D_2 to $y^3S_1^{\circ}$ and the second from a^1G_4 to $w^1F_3^{\circ}$. The spontaneous transitions from $y^3S_1^{\circ}$ level to the a^3P_2 , a^3P_1 , and a^3P_0 levels

correspond to the Ti atomic spectra at 372.52, 370.99, and 370.23 nm, respectively, as indicated by triangle symbols in the top panel of Fig. 2(a). The spectrum at the 497.534 nm [triangle symbols in the bottom panel of Fig. 2(a)] is due to the transition from $w^1F_3^{\circ}$ to b^1D_2 . There is also a possibility of an internal transition from $w^1F_3^{\circ}$ to $s^3D_3^{\circ}$ [21], which is confirmed by the fluorescence at 480.54 nm from $s^3D_3^{\circ}$ to c^3P_2 [triangle symbols in the middle

TABLE I. Center wavelength and FWHM of the detected atomic and ionic spectral lines compared with the NIST database [24]. The term “R” stands for the resonant atomic emission.

Line type	Center wavelength (nm)	FWHM (nm)	Ritz wavelength in air (NIST) (nm)
Ionic line	368.52	0.13	368.51814/368.51963
Atomic line (R)	370.22	0.12	370.22890
Atomic line (R)	370.99	0.12	370.99563
Atomic line (R)	372.51	0.12	372.51533
Ionic line	375.95	0.13	375.92915
Ionic line	376.15	0.14	376.1320
Atomic line (R)	480.52	0.12	480.54144
Atomic line (R)	497.52	0.18	497.53431
Atomic line	498.17	0.10	498.17305
Atomic line	499.11	0.10	499.10660
Atomic line	499.95	0.10	499.95030
Atomic line	500.72	0.11	500.72093
Atomic line	501.44	0.12	501.42762

panel of Fig. 2(a)]. In the observed spectral range, no ionic emissions are identified to be resonantly excited. Benefited from the resonance excitation, the resonance-enhanced atomic emissions are 1 order of magnitude stronger than the nonresonant atomic emissions from 498 to 502 nm.

For this one-dimensional spectral measurement, the laser line locates at the height of 6.5 mm above the burner ($z = 6.5$ mm). As illustrated in Fig. 2(b), the gaseous precursor converts to nanoparticles at the laminar flame sheet. Thus, the titanium in the central zone (zone I) exists as the gaseous precursor and transforms into nanoparticles in the outer zone (zone II), as shown in Fig. 2(a). Both nonresonant and resonance-enhanced emissions clearly exist in zone II but can hardly be found in zone I. Therefore, the spectra can visualize the gas-to-particle conversion across the thin flame surface. Note that the interband absorption coefficient α for nanoparticles can be expressed as $C(h\nu - E_g)^{0.5}$ [25]. When the nanoparticle bandgap E_g increases, the absorption rate decreases significantly. Previous studies [27,28] indicated that the bandgap of nanoparticles increases significantly with the decreasing particle size due to the so-called quantum size effect. Based on an effective mass model [28], the TiO_2 nanoparticle bandgap is about 3.2 eV at 6 nm and increases to about 4.5 eV at 1 nm. Because of the size-dependent bandgap, smaller nanoparticles are more difficult to absorb the laser energy. According to the above analysis of Eq. (1), laser ablation of nanoparticles does not occur for small clusters, which leads to the phase-selective spectra that can be used to trace the nanoparticle formation in reactive flows.

Temporal evolution of the atomic and ionic emissions is examined in order to better understand the spectra. The time-resolved signal of gas Rayleigh scattering is measured to mark the laser pulse. As shown in Fig. 3, both the ionic emission near 376 nm and the resonance-enhanced atomic emission at 480.54 nm decay simultaneously with the laser pulse, while the nonresonant atomic emission at 498.17 nm shows a second peak after the laser pulse. The spontaneous emission lifetimes of both the resonance-enhanced atomic emission and the ionic emission are estimated to be about 10¹ ns based on the Einstein coefficient [23], which, however, cannot explain the fast decays. Thus, the spontaneous emission should not dominate the de-excitation of atoms in the nanoplasmas. Considering the presence of the second peak of the nonresonant atomic emissions, the fast decay of the ionic emission indicates a recombination process through quenching. The recombination process may serve as a new route of populating high-energy states of atoms. The characteristic twin peak of atomic emissions is also observed in the laser-induced atomic emissions of silicon nanoparticles [29,30], but further investigations of the nanoplasma evolution are still needed. For the resonance-enhanced atomic emission, the excited atoms could be de-excited through the stimulated

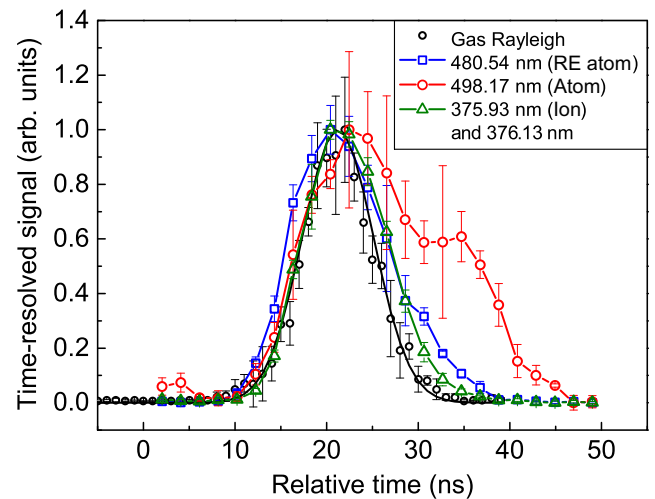


FIG. 3. Time-resolved measurements of the spectra. In the legend, “RE atom,” “Ion,” and “Atom” indicate the resonance-enhanced atomic emission, the ionic emission, and the nonresonant atomic emission, respectively. The Rayleigh signals are fitted by a Gaussian distribution (black line). Each data point comes from the integration result of 200 shots and three sets of measurements are performed to obtain the standard deviations. The gate is 2 ns for the Rayleigh signals and 5 ns for the atomic and ionic emissions.

emission, which is later validated by its saturation feature with the laser intensity.

The dependence of the atomic and ionic emissions on laser intensity is further investigated. Figure 4 shows the signal intensity variations as a function of laser intensity for resonance-enhanced atomic emissions at 480.54 and

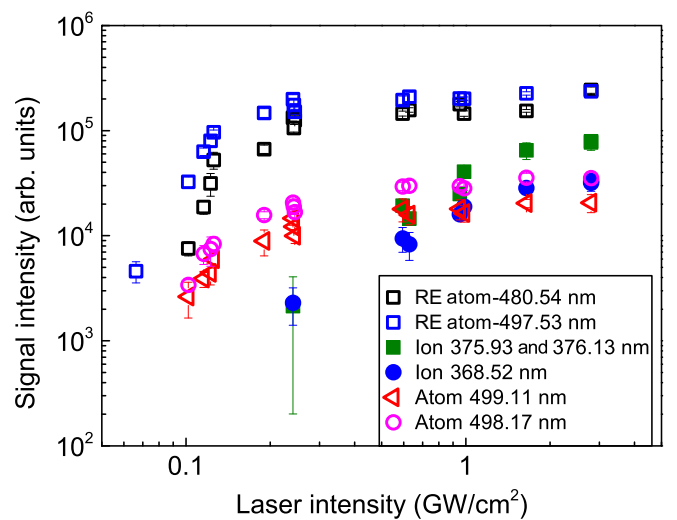


FIG. 4. Dependence of signal intensity on laser intensity. The signal intensity is obtained by integrating the spectra. In the legend, “RE atom,” “Ion,” and “Atom” indicate the resonance-enhanced atomic emission, the ionic emission, and the nonresonant atomic emission, respectively.

497.53 nm, the ionic emissions at 375.93 and 368.52 nm, and the nonresonant atomic emissions at 499.11 and 502.00 nm. All spectra increase with the laser intensity and tend to saturation. For the ionic emissions, the signal intensity can be regarded as the ionization degree of nanoplasmas. Thus, the saturated ionic emission is attributed to the saturated excited electrons with increasing laser intensities [17]. It should be noted that, the laser intensity at which the nonresonant atomic emissions start to saturate is significantly lower for the 355 nm laser ($0.2\text{--}0.3 \text{ GW/cm}^2$) than for the 532-nm laser (1 GW/cm^2) [20]. This result validates that the direct absorption for the 355-nm laser pulse is much more efficient than the two-photon absorption for the 532-nm laser pulse.

For the resonance-enhanced atomic emissions, the plateau tendency of the signal intensity with the laser intensity is caused by the saturation of both nanoparticle ablation and the subsequent resonant excitation. By selecting the laser wavelength consistent with the absorption line of Ti atoms, the resonance-enhanced atomic emissions can easily reach the saturated regime at a signal intensity 1 order of magnitude higher than the nonresonant atomic emissions and the ionic emissions. This feature is of great benefit for the instantaneous two-dimensional imaging of nanoparticle distributions. In the saturation conditions, the stimulated emission is much stronger than the collisional quenching and the spontaneous emission, and thus dominates the de-excitation of excited atoms, according to the classical laser-induced fluorescence theory [31]. The saturated resonance-enhanced atomic emission s_F is proportional to the number density of titanium atoms at the ground state n_0 and the spontaneous emission coefficient

A_{ki} , i.e., $s_F \propto n_0 \times A_{ki}$. Considering the complete ablation of the nanoparticles, the resonance-enhanced atomic emission obeys the relation,

$$s_F \propto n_p V_p A_{ki} \propto \phi_{\text{PVF}} A_{ki}, \quad (2)$$

where n_p is the particle number density, V_p is the averaged nanoparticle volume. This expression predicts a proportional relation between the resonance-enhanced PS-LIBS signal and the particle volume fraction ϕ_{PVF} .

The above relation is validated by measuring the two-dimensional resonance-enhanced atomic emissions at 480.54 nm with the laser intensity of 0.2 GW/cm^2 under different particle volume fractions. In the nanoparticle-laden flow, we can adjust the particle volume fraction by changing the precursor loading rates and keeping the flow condition unchanged. Figure 5(a) shows the signal intensity $I_{\text{PS-LIBS}}$ versus the particle volume fraction ϕ_{PVF} , both of which are averaged in a region of $r = 0 \sim 3 \text{ mm}$ and $z = 53 \sim 63 \text{ mm}$. Since the gas precursor has fully converted into the nanoparticles in this region, the averaged particle volume fraction can be calculated based on the precursor concentration. As predicted, the RE PS-LIBS signal is proportional to the particle volume fraction, which can be described by the correlation $I_{\text{PS-LIBS}}(\text{arb. units}) = 9.995 \phi_{\text{PVF}}(\text{ppb})$. The two-dimensional resonance-enhanced PS-LIBS image is also directly compared with the simulated particle volume fraction by solving a convection-diffusion-reaction equation coupled with a population balance model of nanoparticles in the laminar flow condition. Details about the simulation are given in the Supplemental Material [23,32–34].

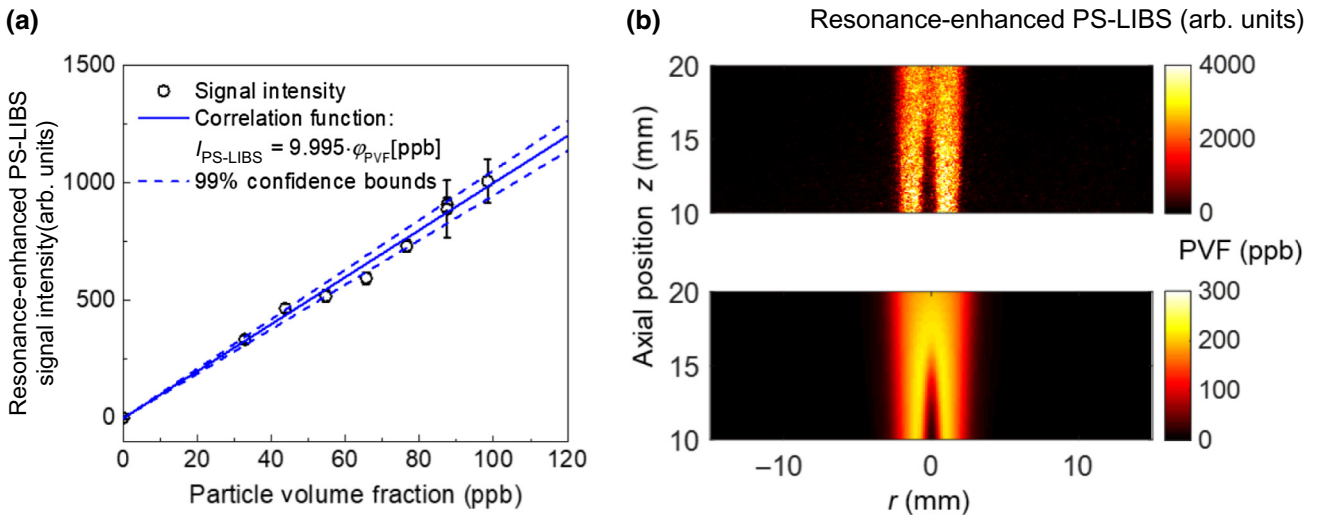


FIG. 5. (a) Dependence of the resonance-enhanced PS-LIBS signal intensities $I_{\text{PS-LIBS}}$ on the particle volume fraction ϕ_{PVF} (black circles) with the proportional correlation function (blue curve) and the 99% confidence bounds for prediction (nonsimultaneous functional bounds); (b) comparison between the two-dimensional resonance-enhanced PS-LIBS snapshots and the simulated particle volume fraction in the laminar flame condition with the precursor loading rate of 0.012 g/min . The origin of the axial position is defined at the burner outlet as shown in Fig. 1(a).

As shown in Fig. 5(b), the resonance-enhanced PS-LIBS image demonstrates a rapid gas-to-particle conversion across the flame sheet, which agrees well with the simulated particle volume fraction. In the postflame region, the signal remains uniform, indicating the conservation of particle volume fraction during the nanoparticle coagulation process.

B. *In situ* two-dimensional diagnostic of nanoparticles

The resonance-enhanced PS-LIBS is further applied to measure TiO_2 particle volume fraction in the turbulent condition, in combination with the simultaneous OH PLIF measurement. Figure 6(a) illustrates instantaneous two-dimensional distributions of the particle volume fractions and OH radicals at the different ranges of axial positions from 10 to 70 mm. Figure 6(b) shows the averaged results from 100 snapshots. The turbulent reactive zone can be divided into two regions based on the instantaneous OH PLIF, (1) a laminar region from the nozzle outlet to the axial position of 25 mm where the wrinkled flame is anchored at the burner outlet, and downstream (2) a turbulent region with the turbulent diffusion flame brush.

In the laminar region, the TiO_2 nanoparticles concentrate inside the OH radical zone and form an annular layer. This distribution indicates the generation of nanoparticles near the flame-reaction surface. Since the OH radicals usually exist at the flame-reaction zone, the gas-to-particle conversion of TiO_2 occurs earlier than the appearance of OH radicals before the stoichiometric flame surface. This phenomenon, observed also in the large-eddy simulation of TiO_2 nanoparticles by Sung *et al.* [35], is

caused by the fast hydrolysis reaction of the precursor TTIP with H_2O molecules and radicals generated near the stoichiometric reaction surface. The nanoparticles are mainly transported downstream by convection, rather than diffusing across the reaction layer owing to the large Peclet number.

In the turbulent region, the nanoparticle-concentrated layer breaks into thin structures with a strong correlation with the OH radical distribution. This feature is significantly different from that in the laminar region. A similar phenomenon has also been observed in the soot inception of turbulent flames based on LII measurements [36,37]. This nanoparticle formation pattern is attributed to the radical-driven feature of precursor reactions [32]. The precursor reactions can thus be strongly affected by the turbulent reactive flow, implying a strong coupling between precursor chemistry and turbulence.

The nanoparticle formation and transport at different flow conditions are also investigated to verify this viewpoint. The increase in the co-flow rate leads to a higher shear rate and thus larger turbulence intensity. As illustrated by the distribution of OH radicals in Fig. 7(a), when the flow velocity exceeds 6.5 m/s, the laminar flow region transits to turbulent regime due to the enhanced Kelvin-Helmholtz instability [38]. Because of the changes in the reactive flow structure, the wrinkled layers of TiO_2 nanoparticles also transit from annular layers to distorted turbulent structures. To understand the correlation between nanoparticle pattern and the turbulent flow structure, we calculate the cross-correlation function K between the particle volume fraction and OH distributions, defined as

$$K(\delta_r, \delta_z) = \frac{\sum_z \sum_r \left[I_{\text{PVF}}(r, z) - \overline{I}_{\text{PVF}}(r, z) \right] \left[I_{\text{OH}}(r + \delta_r, z + \delta_z) - \overline{I}_{\text{OH}}(r + \delta_r, z + \delta_z) \right]}{(N_z - |\delta_z| - 1)(N_r - |\delta_r| - 1)\sigma_{\text{PVF}}\sigma_{\text{OH}}}, \quad (3)$$

where I_{PVF} and I_{OH} are the snapshots of particle volume fraction and OH radical with the axial length of N_z and radial length of N_r , and δ_r and δ_z are the displacement variables in the radial and axial directions, respectively. The particle volume fraction and OH snapshots are subtracted by their mean values ($\overline{I}_{\text{PVF}}$ and \overline{I}_{OH} , respectively) and then normalized by the standard deviations σ_{PVF} and σ_{OH} evaluated in the cross-correlation region ($N_r - |\delta_r|$) \times ($N_z - |\delta_z|$) in order to eliminate boundary effects. Thus, the cross-correlation function $K(\delta_r, \delta_z)$ ranges from -1 to 1 , which corresponds to anticorrelation and perfect correction. Figure 7(b) shows averaged $K(\delta_r, \delta_z)$ for 100 pairs of images at different co-flow velocities. In laminar flame conditions, with the co-flow velocities of 2.6

and 4.3 m/s, the particle volume fractions and the OH radicals are closely correlated at two layers with nonzero displacements. This correlation indicates that the nanoparticle formation and transport are controlled by the outer reaction layer. As the co-flow velocity further increases, the cross-correlation function maximizes at the zero displacements, representing a spatial correlation between the particle volume fractions and OH radicals.

Figure 8 depicts the correlation function with zero displacements $K(0, 0)$ at different co-flow velocities, i.e., the cosine similarity of the particle volume fractions and the OH radicals. By increasing the co-flow velocity, the particle volume fractions correlate more closely with the OH radicals. When the co-flow velocity reaches 10 m/s,

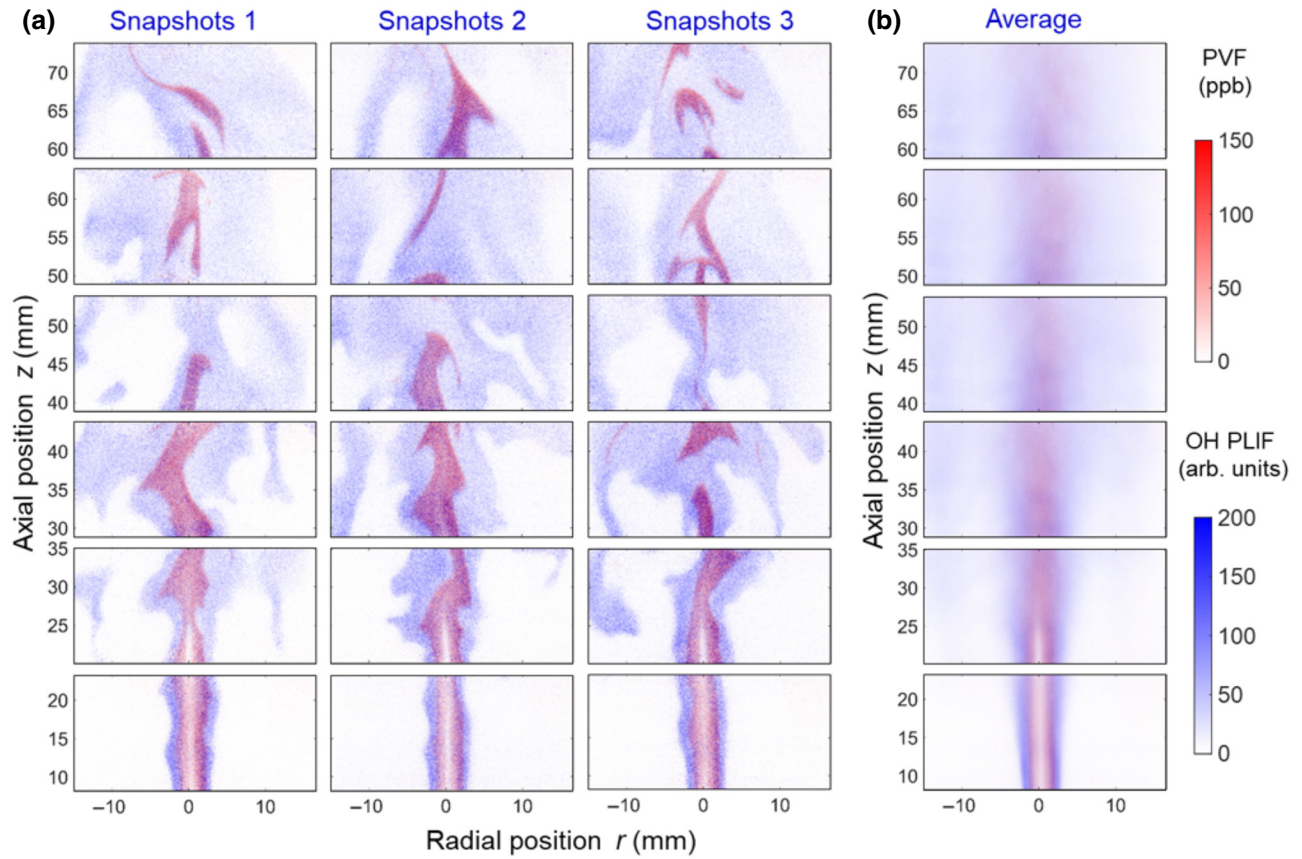


FIG. 6. Simultaneous resonance-enhanced PS-LIBS and PLIF measurements of particle volume fractions and OH at different axial positions, (a) three snapshots, (b) averaged image. The signal-to-noise ratios are 239 for the resonance-enhanced PS-LIBS signal and 45 for OH PLIF (based on the maximum signal).

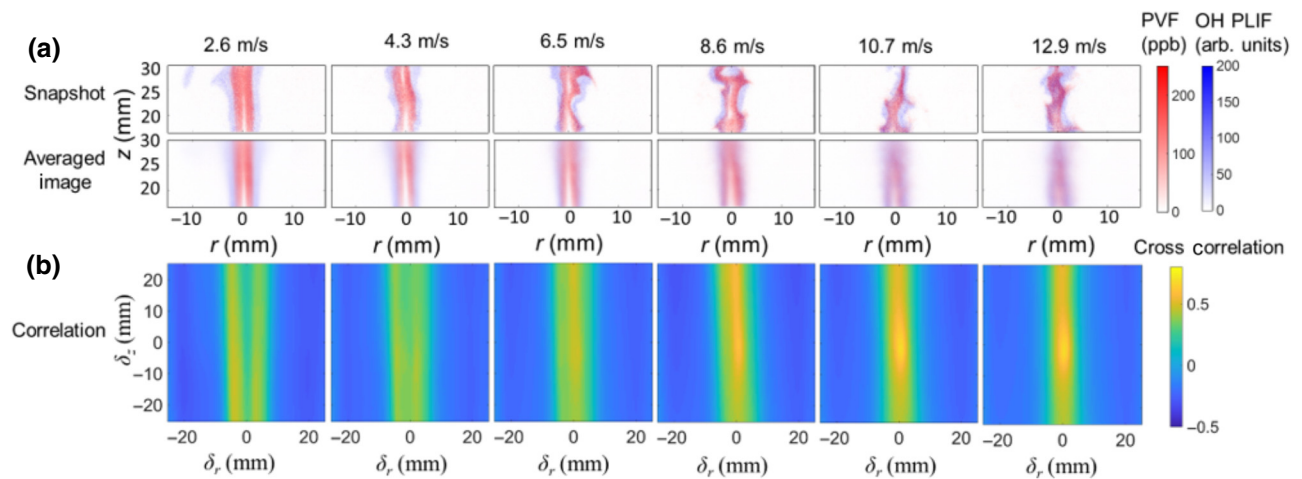


FIG. 7. Simultaneous two-dimensional resonance-enhanced PS-LIBS and PLIF measurements with different co-flow velocities while keeping the central jet flow constant.

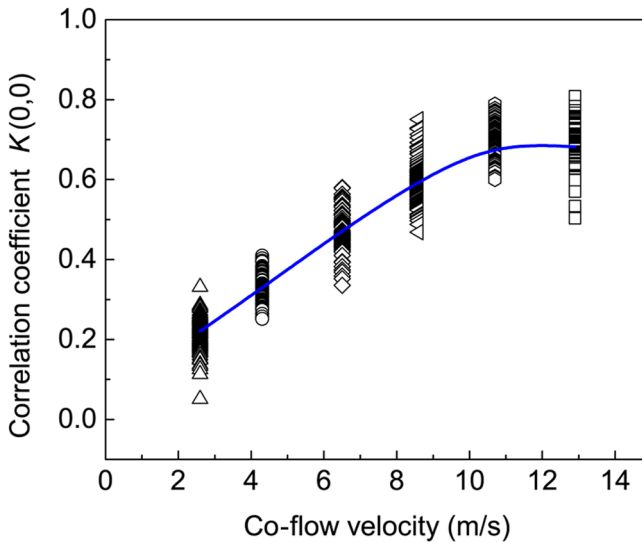


FIG. 8. Correlation coefficients $K(0,0)$ at different co-flow velocities, where the scatters indicate the correlation factors of 100 snapshots and the blue curve indicates the average $K(0,0)$.

the correlation function reaches a saturation level. Under this condition, the TiO_2 nanoparticle pattern is largely dominated by the turbulent flame structure. As the co-flow velocity increases, the characteristic turbulent time scale (τ_{flow}) decreases significantly due to the enhanced Kelvin-Helmholtz instability at higher shear rates, whereas the characteristic reaction time of TTIP precursor (τ_{chem}) is less influenced by the flow structure [32,39]. As the ratio of τ_{flow} and τ_{chem} increases, the precursor consumption is gradually controlled by the turbulent reactive flow, confirming the closer correlation between the particle volume fraction and OH radicals.

IV. CONCLUSION

In this work, we present a resonance-enhanced PS-LIBS technique for instantaneous two-dimensional imaging of nanoparticle formation and transport in turbulent reactive flows. The resonance-enhanced PS-LIBS is characterized to be a two-step process: (1) the direct absorption of 355-nm laser pulses induces the ablation of TiO_2 nanoparticles and the formation of nanoplasma; (2) the same laser pulse further excites the metastable Ti atoms in the nanoplasma inducing the resonance-enhanced atomic emissions. The generated resonance-enhanced atomic emission, i.e., the resonance-enhanced PS-LIBS signal, is 1 order of magnitude stronger than the nonresonant atomic emission, i.e., the PS-LIBS signal. The theoretical analysis suggests that the resonance-enhanced PS-LIBS can allow for quantitative *in situ* measurements of particle volume fractions with phase selectivity. Then, the proportional relation between the signal intensity and the particle volume fraction is established and validated in the laminar flow condition. In

combination with the simultaneous OH PLIF measurement in the turbulent reactive flow, the instantaneous imaging of particle volume fraction based on resonance-enhanced PS-LIBS reveals the nanoparticle formation patterns in both laminar and turbulent regions. In the laminar region, the nanoparticles form and concentrate at the inner layer of the gas-reaction zone, indicating a fast precursor hydrolysis reaction. In the turbulent region, the nanoparticles correlate with the gas species of the turbulent reactive flow, indicating the precursor chemistry-turbulence coupling. At higher co-flow velocities, the precursor consumption is gradually dominated by the turbulent reactive flow due to the enhanced turbulence at higher shear rates.

ACKNOWLEDGMENTS

This work is mainly funded by the National Natural Science Funds of China [Grants No. 51725601 and No. 51676109]. The authors would like to acknowledge Heinz Pitsch from RWTH-Aachen, Stephen D. Tse from Rutgers, Christof Schulz from Duisburg-Essen, Qiang Yao and Yi-Kang Pu from Tsinghua for valuable discussions, as well as Kai Hong Luo from Tsinghua and Yun Huang from Chinese Academy of Sciences for their helps on experimental facilities. Y.R. also thanks the support from the Alexander von Humboldt Foundation.

APPENDIX A: ONE-DIMENSIONAL SPECTRAL DATA

Table I lists the center wavelength and FWHM of the detected atomic and ionic spectral lines compared with the NIST database.

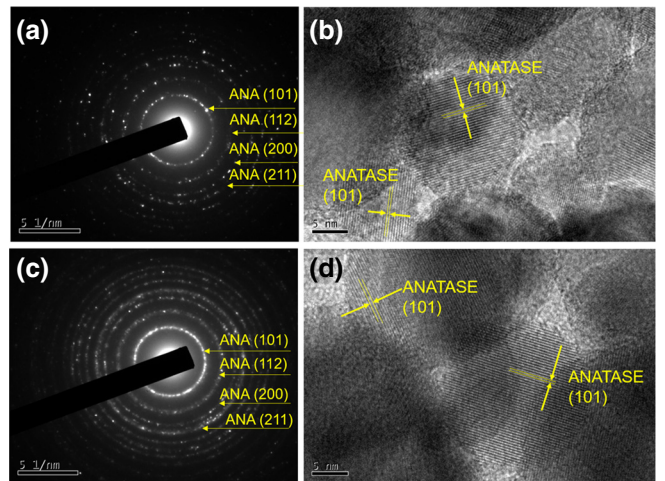


FIG. 9. Diffraction patterns and TEM pictures of flame-synthesized TiO_2 nanoparticles in the laminar (a),(b) and turbulent (c),(d) conditions.

APPENDIX B: CHARACTERIZATION OF THE SYNTHESIZED NANOPARTICLES

Figure 9 shows the diffraction patterns and TEM images of the TiO₂ nanoparticles in both laminar and turbulent conditions. The nanoparticles have the anatase crystalline, as identified by the diffraction patterns as well as the dominated (1 0 1) lattice plane of anatase in the TEM images. Compared with other TiO₂ polymorphs, the anatase crystal structure is favored for photocatalysts due to the low bandgap [40]. By statistically counting 100 nanoparticles from TEM images, the average particle size is measured as 29.1 nm with the geometric standard deviation of 1.36 in the laminar condition, while the average size is 30.9 nm with the geometric standard deviation of 1.50 in the turbulent condition.

- [1] K. O. Johansson, M. P. Head-Gordon, P. E. Schrader, K. R. Wilson, and H. A. Michelsen, Resonance-stabilized hydrocarbon-radical chain reactions may explain soot inception and growth, *Science* **361**, 997 (2018).
- [2] V. L. Hartwick, O. B. Toon, and N. G. Heavens, High-altitude water ice cloud formation on Mars controlled by interplanetary dust particles, *Nat. Geosci.* **12**, 516 (2019).
- [3] C. D. O'Dowd, P. Aalto, K. Hämeri, M. Kulmala, and T. Hoffmann, Atmospheric particles from organic vapours, *Nature* **416**, 497 (2002).
- [4] P. Shukla and A. Mamun, *Introduction to Dusty Plasma Physics* (CRC press, Boca Raton, 2015).
- [5] S. Li, Y. Ren, P. Biswas, and S. D. Tse, Flame aerosol synthesis of nanostructured materials and functional devices: Processing, modeling, and diagnostics, *Prog. Energy Combust. Sci.* **55**, 1 (2016).
- [6] W. Y. Teoh, R. Amal, and L. Mädler, Flame spray pyrolysis: An enabling technology for nanoparticles design and fabrication, *Nanoscale* **2**, 1324 (2010).
- [7] A. M. Morales and C. M. L. Lieber, A laser ablation method for the synthesis of crystalline semiconductor nanowires, *Science* **279**, 208 (1998).
- [8] E. Garwin, S. Schwyn, and A. Schmidt-Ott, Aerosol generation by spark discharge, *J. Aerosol. Sci.* **19**, 639 (1988).
- [9] J. Menser, K. Daun, T. Dreier, and C. Schulz, Laser-induced incandescence from laser-heated silicon nanoparticles, *Appl. Phys. B-Lasers Opt.* **122**, 277 (2016).
- [10] F. Cignoli, C. Bellomunno, S. Maffi, and G. Zizak, Laser-induced incandescence of titania nanoparticles synthesized in a flame, *Appl. Phys. B Lasers Opt.* **96**, 593 (2009).
- [11] J. Y. Hwang, Y. S. Gil, J. I. Kim, M. Choi, and S. H. Chung, Measurements of temperature and OH radical distributions in a silica generating flame using CARS and PLIF, *J. Aerosol. Sci.* **32**, 601 (2001).
- [12] G. Beaucage, H. K. Kammler, R. Mueller, R. Strobel, N. Agashe, S. E. Pratsinis, and T. Narayanan, Probing the dynamics of nanoparticle growth in a flame using synchrotron radiation, *Nat. Mater.* **3**, 370 (2004).
- [13] M. N. Shneider and S. F. Gimelshein, Application of coherent Rayleigh-Brillouin scattering for in situ nanoparticle and large molecule detection, *Appl. Phys. Lett.* **102**, 173109 (2013).
- [14] A. Gerakis, Y. W. Yeh, M. N. Shneider, J. M. Mitrani, B. C. Stratton, and Y. Raitses, Four-Wave-Mixing Approach to In Situ Detection of Nanoparticles, *Phys. Rev. Appl.* **9**, 14031 (2018).
- [15] N. G. Glumac, Formation and consumption of SiO in powder synthesis flames, *Combust. Flame* **124**, 702 (2001).
- [16] Y. Zhang, G. Xiong, S. Li, Z. Dong, S. G. Buckley, and S. D. Tse, Novel low-intensity phase-selective laser-induced breakdown spectroscopy of TiO₂ nanoparticle aerosols during flame synthesis, *Combust. Flame* **160**, 725 (2013).
- [17] Y. Zhang, S. Li, Y. Ren, Q. Yao, and C. K. Law, Two-dimensional imaging of gas-to-particle transition in flames by laser-induced plasmas, *Appl. Phys. Lett.* **104**, 023115 (2014).
- [18] Y. Ren, Y. Zhang, S. Li, and C. K. Law, Doping mechanism of Vanadia/Titania nanoparticles in flame synthesis by a novel optical spectroscopy technique, *Proc. Combust. Inst.* **35**, 2283 (2015).
- [19] Y. Zhang, S. Li, Y. Ren, Q. Yao, and S. D. Tse, A new diagnostic for volume fraction measurement of metal-oxide nanoparticles in flames using phase-selective laser-induced breakdown spectroscopy, *Proc. Combust. Inst.* **35**, 3681 (2015).
- [20] Y. Ren, S. Li, Y. Zhang, S. D. Tse, and M. B. Long, Absorption-Ablation-Excitation Mechanism of Laser-Cluster Interactions in a Nanoaerosol System, *Phys. Rev. Lett.* **114**, 093401 (2015).
- [21] G. Xiong, S. Li, Y. Zhang, S. G. Buckley, and S. D. Tse, Phase-selective laser-induced breakdown spectroscopy of metal-oxide nanoparticle aerosols with secondary resonant excitation during flame synthesis, *J. Anal. At. Spectrom.* **31**, 482 (2016).
- [22] G. Xiong, S. Li, and S. D. Tse, Tuning excitation laser wavelength for secondary resonance in low-intensity phase-selective laser-induced breakdown spectroscopy for in-situ analytical measurement of nanoaerosols, *Spectroc. Acta Pt. B-Atom. Spectr.* **140**, 13 (2018).
- [23] See Supplemental Material at <http://link.aps.org/supplemental/10.1103/PhysRevApplied.13.044002> for the experimental setup, spectroscopy information, and the numerical model for nanoparticle synthesis.
- [24] A. Kramida, Y. Ralchenko, J. Reader, and NIST ASD Team, NIST Atomic Spectra Database [Online]. (National Institute of Standards and Technology, Gaithersburg, MD), <https://physics.nist.gov/asd> (retrieved 2019).
- [25] B. E. A. Saleh and M. C. Teich, in *Fundamentals of Photonics* (John Wiley & Sons, Inc., New York, 1991).
- [26] L. Kernazhitsky, V. Shymanovska, T. Gavrilko, V. Naumov, and V. Kshnyakin, Optical absorption of polydisperse TiO₂: Effect of surface doping by transition metal cations, *Ukr. J. Phys. Opt.* **14**, 15 (2013).
- [27] L. E. Brus, Electron-electron and electron-hole interactions in small semiconductor crystallites: The size dependence of

- the lowest excited electronic state, *J. Chem. Phys.* **80**, 4403 (1984).
- [28] Y. Wang and N. Herron, Nanometer-sized semiconductor clusters: Materials synthesis, quantum size effects, and photophysical properties, *J. Phys. Chem.* **95**, 525 (1991).
- [29] K. Daun, J. Menser, R. Mansmann, S. T. Moghadam, T. Dreier, and C. Schulz, Spectroscopic models for laser-heated silicon and copper nanoparticles, *J. Quant. Spectrosc. Radiat. Transfer* **197**, 3 (2017).
- [30] J. Menser, K. Daun, T. Dreier, and C. Schulz, Laser-induced atomic emission of silicon nanoparticles during laser-induced heating, *Appl. Opt.* **56**, E50 (2017).
- [31] A. C. Eckbreth, *Laser Diagnostics for Combustion Temperature and Species* (CRC Press, Boca Raton, 1996).
- [32] A. G. Shmakov, O. P. Korobeinichev, D. A. Knyazkov, A. A. Paletsky, R. A. Maksutov, I. E. Gerasimov, T. A. Bolshova, V. G. Kiselev, and N. P. Gritsan, Combustion chemistry of $Ti(OC_3H_7)_4$ in premixed flat burner-stabilized H₂/O₂/Ar flame at 1 atm, *Proc. Combust. Inst.* **34**, 1143 (2013).
- [33] P. Buerger, D. Nurkowski, J. Akroyd, and M. Kraft, A kinetic mechanism for the thermal decomposition of titanium tetraisopropoxide, *Proc. Combust. Inst.* **36**, 1019 (2017).
- [34] H. G. Weller, G. Tabor, H. Jasak, and C. Fureby, A tensorial approach to computational continuum mechanics using object-oriented techniques, *Comput. Phys.* **12**, 620 (1998).
- [35] Y. Sung, V. Raman, and R. O. Fox, Large-eddy-simulation-based multiscale modeling of TiO₂ nanoparticle synthesis in a turbulent flame reactor using detailed nucleation chemistry, *Chem. Eng. Sci.* **66**, 4370 (2011).
- [36] F. Bisetti, G. Blanquart, M. E. Mueller, and H. Pitsch, On the formation and early evolution of soot in turbulent nonpremixed flames, *Combust. Flame* **159**, 317 (2012).
- [37] N. H. Qamar, Z. T. Alwahabi, Q. N. Chan, G. J. Nathan, D. Roekaerts, and K. D. King, Soot volume fraction in a piloted turbulent jet non-premixed flame of natural gas, *Combust. Flame* **156**, 1339 (2009).
- [38] A. J. Yule, N. A. Chigier, S. Ralph, J. R. Boulder, and J. Ventura, Combustion-transition interaction in a jet flame, *AIAA J.* **19**, 752 (1981).
- [39] G. P. Klaassen and W. R. Peltier, The onset of turbulence in finite-amplitude Kelvin-Helmholtz billows, *J. Fluid Mech.* **155**, 1 (1985).
- [40] S. Memarzadeh, E. D. Tolmachoff, D. J. Phares, and H. Wang, Properties of nanocrystalline TiO₂ synthesized in premixed flames stabilized on a rotating surface, *Proc. Combust. Inst.* **33**, 1917 (2011).